Design and Comparison of Two Control Strategies for Voltage-sag Compensation using Dynamic Voltage Restorers

A. P. Torres[1], P. Roncero-Sanchez[2], X. del Toro Garcia[2], V. Feliu[2]
[1]*Robotics and Automation Centre, Albacete Science and Technology Park, Paseo de la Innovación 1, 02006 Albacete, Spain*
[2]*Department of Electrical, Electronics, Control Engineering and Communications, University of Castilla-La Mancha, Campus Universitario S/N, 13071 Ciudad Real, Spain*
alfonso.parreno@pcyta.com

***Abstract*—The Dynamic Voltage Restorer (DVR) is one of the most frequently used devices for voltage-sag compensation. This work explains the design procedure and comparison of two different control strategies for the compensation of balanced and imbalanced voltage sags by using a DVR. The two strategies considered are the widely-used proportional-integral (PI) controller and a new approach based on the generalized proportional-integral (GPI) controller. Both control schemes are implemented in a synchronous reference frame (SRF) and use a feedforward term to improve the time response. The simulations in PSCAD/EMTDC show the performance of both control strategies for several voltage sags and for grid-frequency deviations. The obtained results show that the SRF-GPI approach is superior.**

***Index Terms*—Control design, dynamic voltage restorer, power quality, voltage sag.**

I. INTRODUCTION

The most frequent power quality disturbances which affect electrical grids include voltage sags, swells and harmonics. These disturbances have a negative impact on the electrical grid and the equipment connected to it, causing economical losses, poor efficiency and safety issues. Research efforts have been developed in recent decades to mitigate these effects using custom power devices [1]. The Dynamic Voltage Restorer (DVR) is a high-performance solution to compensate voltage disturbances in sensitive loads, providing very fast dynamics and a cost-effective solution when compared to UPS systems. The DVR is particularly suitable for short duration disturbances such as voltage sags rather than long interruptions, which require large energy storage systems.

Manuscript received January 24, 2013; accepted April 7, 2013.

This work has been partially supported in part by the Ministry of Economy and Competitiveness of Spain under the research project ENE2012-33541, in part by Ministry of Economy and Competitiveness of Spain in the framework of the National Program of Scientific Research, Development and Technological Innovation (2008-2011), in part by the European Regional Development Fund under the Research Project IPT-2011-1468-920000.

Xavier del Toro García has been supported by the "Juan de la Cierva" program (JCI-2011-10371) of the Ministry of Economy and Competitiveness of Spain.

The typical configuration of a power system including a DVR is shown in Fig. 1. As it can be seen, the DVR is connected in series between the point of common coupling (PCC) and a sensitive load. It generally consists of four different components [2]: an energy storage system or an alternative power source, a voltage source converter (VSC) which converts the DC voltage from the energy storage system to the required AC voltage to cancel out disturbances, a coupling transformer which is series connected in the line and an output filter to cancel the harmonics introduced by the PWM process of the VSC.

Regarding the control of the DVR, the simplest solution is a feedforward term based on the difference between the grid voltage and the load reference voltage. However, this solution can produce nonzero tracking errors due to the dynamics of the output filter. The performance of the control can be improved by using a closed-loop scheme to reduce the tracking error of the reference, and it can additionally include an active damping of the resonant frequency of the output filter to enhance the stability of the system. Many different closed-loop strategies for compensating voltage sags using a DVR can be found in literature. The most widely used is the proportional-integral (PI) controller in a synchronous reference frame (SRF) [3], but recently other schemes with additional features have been proposed, such as proportional-resonant controllers [4] and repetitive controllers [5], which can deal with harmonic compensation and avoid the requirement of a synchronization method to perform the coordinate transformations since they are implemented in a stationary reference frame. Nevertheless, the main drawback of these methods is their sensitivity to frequency variations, because the value of the grid frequency is required. Recently, a novel approach based on a generalized proportional-integral (GPI) control [6] has been proposed. This solution enhances the robustness against frequency variations.

This paper is organized as follows. The DVR modeling is presented in Section II. The design procedure for the SRF-GPI and SRF-PI controllers is explained in Section III and Section IV, respectively. Section V shows the performance of the both control schemes in PSCAD/EMTDC simulations. Finally, the conclusions are given in Section VI.

II. MODEL OF THE DVR

Although a VSC has a nonlinear nature due to its switching operation, it will be considered as a linear amplifier under the assumption of a high switching frequency [7]. In this situation, the DVR can be modeled as an ideal voltage source connected to an LC filter. Since the controllers will be implemented in a SRF, the resulting state-space model of the DVR shown in Fig. 1 is

$$\frac{d}{dt}\begin{bmatrix} v_{\mathrm{cd}} \\ v_{\mathrm{cq}} \\ i_{L_{\mathrm{f}}\mathrm{d}} \\ i_{L_{\mathrm{f}}\mathrm{q}} \end{bmatrix} = \mathbf{A_1}\begin{bmatrix} v_{\mathrm{cd}} \\ v_{\mathrm{cq}} \\ i_{L_{\mathrm{f}}\mathrm{d}} \\ i_{L_{\mathrm{f}}\mathrm{q}} \end{bmatrix} + \mathbf{B_1}\begin{bmatrix} i_{\mathrm{sd}} \\ i_{\mathrm{sq}} \\ u_{\mathrm{d}} \\ u_{\mathrm{q}} \end{bmatrix}, \tag{1}$$

with

$$\mathbf{A_1} = \begin{bmatrix} 0 & \omega_{\mathrm{l}} & \frac{1}{C_{\mathrm{f}}} & 0 \\ -\omega_{\mathrm{l}} & 0 & 0 & \frac{1}{C_{\mathrm{f}}} \\ -\frac{1}{L_{\mathrm{f}}} & 0 & -\frac{R_{\mathrm{f}}}{L_{\mathrm{f}}} & \omega_{\mathrm{l}} \\ 0 & -\frac{1}{L_{\mathrm{f}}} & -\omega_{\mathrm{l}} & -\frac{R_{\mathrm{f}}}{L_{\mathrm{f}}} \end{bmatrix}, \mathbf{B_1} = \begin{bmatrix} -\frac{1}{C_{\mathrm{f}}} & 0 & 0 & 0 \\ 0 & -\frac{1}{C_{\mathrm{f}}} & 0 & 0 \\ 0 & 0 & \frac{1}{L_{\mathrm{f}}} & 0 \\ 0 & 0 & 0 & \frac{1}{L_{\mathrm{f}}} \end{bmatrix}, \tag{2}$$

where L_{f} and R_{f} are the leakage inductance and the copper losses of the transformer, respectively, C_{f} is the output capacitor and ω_{l} is the angular speed of the SRF ($\omega_{\mathrm{l}} = 100\pi$ rad/s); v_{cd} and v_{cq} are the d and q components of the capacitor voltage, which are the variables to be controlled, $i_{L_{\mathrm{f}}\mathrm{d}}$ and $i_{L_{\mathrm{f}}\mathrm{q}}$ are the current components through the leakage inductance, i_{sd} and i_{sq} stand for the current of the load, and u_{d} and u_{q} are the VSC output voltage components.

The components i_{sd} and i_{sq} can be compensated by using the feedforward term $\hat{P}_{\mathrm{l}}^{-1}(s)$, which it is shown in the control schemes depicted in Fig. 2 and Fig. 3. In these schemes, the transfer-function blocks for the model of the plant are

$$P_1(s) = \frac{1}{R_{\mathrm{f}} + L_{\mathrm{f}} s}, P_2(s) = \frac{1}{C_{\mathrm{f}} s}. \tag{3}$$

The whole system can be decoupled by using the following equations [8]:

$$U_{\mathrm{d}}(s) = \left(L_{\mathrm{f}} s + R_{\mathrm{f}}\right) I_{\mathrm{sd}}(s) + W_{\mathrm{cd}}(s) + U_{\mathrm{cd}}(s), \tag{4}$$

$$U_{\mathrm{q}}(s) = \left(L_{\mathrm{f}} s + R_{\mathrm{f}}\right) I_{\mathrm{sq}}(s) + W_{\mathrm{cq}}(s) + U_{\mathrm{cq}}(s), \tag{5}$$

with:

$$W_{\mathrm{cd}}(s) = -\omega_{\mathrm{l}} L_{\mathrm{f}} I_{L_{\mathrm{f}}\mathrm{q}}(s) - \omega_{\mathrm{l}} C_{\mathrm{f}} \left(L_{\mathrm{f}} s + R_{\mathrm{f}}\right) V_{\mathrm{cq}}(s), \tag{6}$$

$$W_{\mathrm{cq}}(s) = \omega_{\mathrm{l}} L_{\mathrm{f}} I_{L_{\mathrm{f}}\mathrm{d}}(s) - \omega_{\mathrm{l}} C_{\mathrm{f}} \left(L_{\mathrm{f}} s + R_{\mathrm{f}}\right) V_{\mathrm{cd}}(s). \tag{7}$$

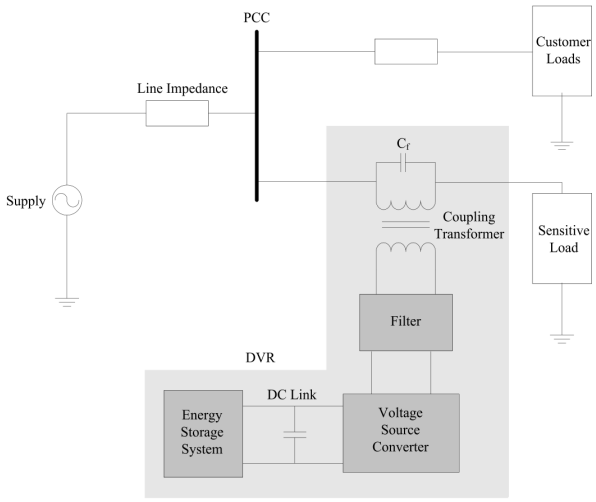

Fig. 1. Scheme of a power system with a DVR.

Then, the generic transfer function in a d-q frame can be expressed as

$$G(s) = \frac{V_c(s)}{U_c(s)} = \frac{\omega_n^2}{s^2 + s2\xi\omega_n + \omega_n^2}, \tag{8}$$

with $U_{\mathrm{c}}(s)$ being the controller output, $\omega_{\mathrm{n}}^2 = 1/(C_{\mathrm{f}} L_{\mathrm{f}})$ and $\xi = \frac{R_{\mathrm{f}}}{2}\sqrt{C_{\mathrm{f}}/L_{\mathrm{f}}}$.

III. DVR CONTROL SCHEME BASED ON A SRF-GPI CONTROLLER

The control strategy based on a SRF-GPI regulator is shown in Fig. 2. The scheme consists of a feed forward compensation (with $K_{\mathrm{f}} = 1$), which speeds up the transient response and a feedback loop with a GPI controller, which reduces the tracking error of the reference. In order to design the control system, the following errors must be defined:

$$e_y(t) = v_{\mathrm{c}}(t) - v_{\mathrm{c}}^*(t), \tag{9}$$

$$e_u(t) = u_{\mathrm{c}}(t) - u_{\mathrm{c}}^*(t). \tag{10}$$

The error $e_y(t)$ is obtained by using (8)

$$\ddot{e}_y(t) + \dot{e}_y(t)2\xi\omega_{\mathrm{n}} + e_y(t)\omega_{\mathrm{n}}^2 = e_u(t)\omega_{\mathrm{n}}^2. \tag{11}$$

From the previous expression, the error derivative can be obtained by means of an integral reconstructor [9] as shown in (12)

$$\hat{\dot{e}}_y(t) = \omega_{\mathrm{n}}^2 \int_0^t e_u(\tau)d\tau - 2\xi\omega_{\mathrm{n}} e_y(t) - \omega_{\mathrm{n}}^2 \int_0^t e_y(\tau)d\tau. \tag{12}$$

A PID control law can be defined in the time domain as

$$e_u(t) = -K_{\mathrm{d}}\dot{e}_y(t) - K_{\mathrm{p}} e_y(t) - K_{\mathrm{i}} \int e_y(\tau)d\tau. \tag{13}$$

The error derivative term of (13) is generally measured, but it can also be estimated as it is done in the GPI control design methodology.

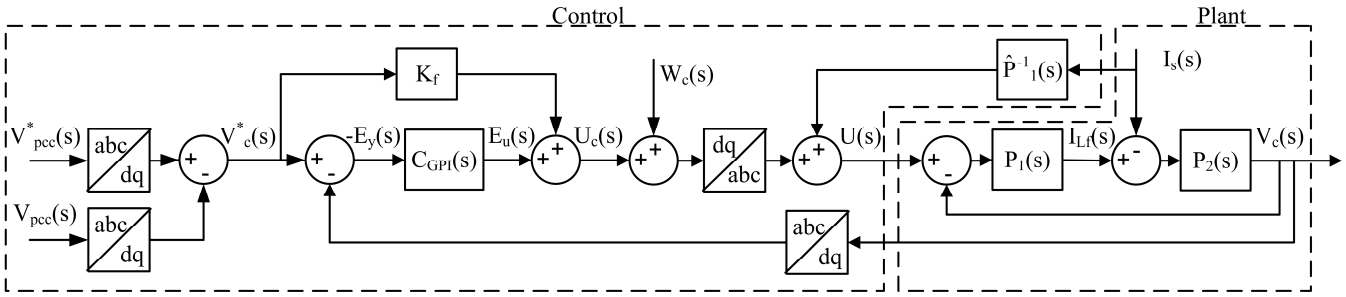

Fig. 2. DVR-voltage closed-loop control scheme based on the SRF-GPI controller.

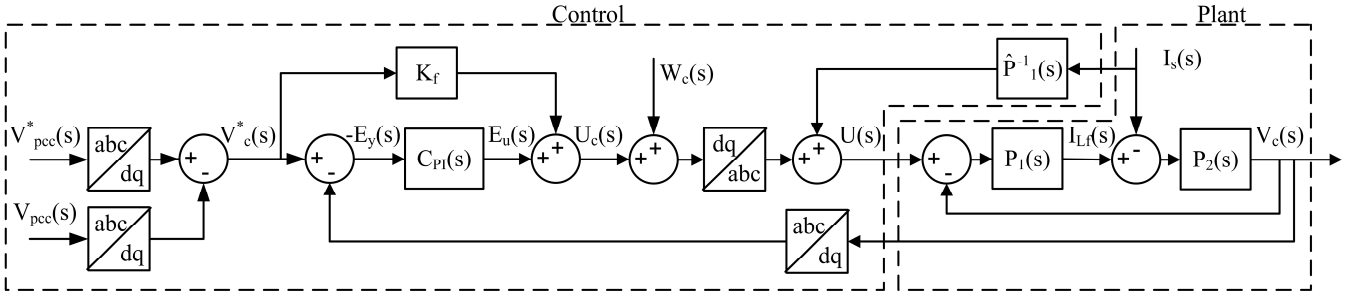

Fig. 3. DVR-voltage closed-loop control scheme based on the SRF-PI controller.

The derivative term can be estimated replacing $\dot{e}_y(t)$ by the integral reconstructor, $\hat{\dot{e}}_y(t)$. Moreover, introducing several consecutive integrals of $e_y(t)$, the error due to the initial conditions and possible disturbances can be reduced. Additionally, the tracking error is improved. In the example developed in Section V, a reasonable tradeoff between tracking accuracy and implementation complexity of the controller is achieved by using three consecutive integrals. Then, the time-domain equation of the GPI controller is

$$\begin{aligned} e_u(t) = &-K_5\int e_u(\tau)d\tau - K_4 e_y(t) - K_3\int e_y(\tau)d\tau - \\ &-K_2\int^{(2)} e_y(\lambda)d\lambda d\tau - K_1\int^{(3)} e_y(\gamma)d\gamma d\lambda d\tau - \\ &-K_0\int^{(4)} e_y(\sigma)d\sigma d\gamma d\lambda d\tau. \end{aligned} \quad (14)$$

It should be noted that only integral terms are present in the new control law. Applying the Laplace transform, the control output is

$$U_c(s) = V_c^*(s) - \underbrace{\left[\frac{s^4K_4 + s^3K_3 + s^2K_2 + sK_1 + K_0}{s^3(s+K_5)}\right]}_{C_{GPI}(s)} E_y(s). \quad (15)$$

The closed-loop transfer function is obtained by combining (15) and (8), which gives the following characteristic polynomial

$$p(s) = s^6 + \alpha_5 s^5 + \alpha_4 s^4 + \alpha_3 s^3 + \alpha_2 s^2 + \alpha_1 s + \alpha_0. \quad (16)$$

The design coefficients can be chosen to obtain a Hurwitz polynomial with the desired roots [10]. If the six roots are considered to be equal ($s = p$), the design coefficients can be calculated as

$$\begin{aligned} &\alpha_5 = -6p, \alpha_4 = 15p^2, \alpha_3 = -20p^3, \\ &\alpha_2 = 15p^4, \alpha_1 = -6p^5, \alpha_0 = p^6. \end{aligned} \quad (17)$$

Fig. 4 shows the root locus of the control scheme and the closed-loop pole location, which are placed at $s = -4200$.

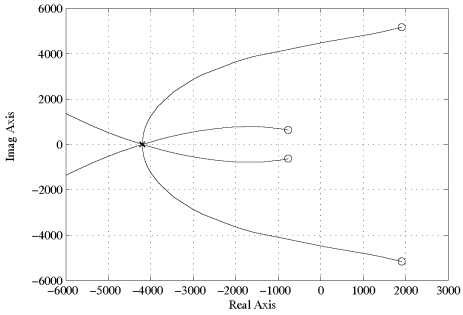

Fig. 4. Root locus plot and closed-loop pole location for the GPI control scheme.

The Bode plot for the closed-loop transfer function including the designed GPI controller is illustrated in Fig. 5.

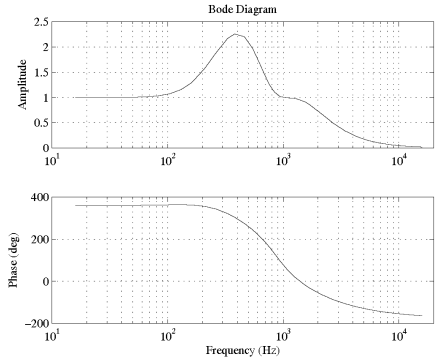

Fig. 5. Bode plot of the closed-loop system for the GPI control scheme.

IV. DVR CONTROL SCHEME BASED ON THE SRF-PI CONTROLLER

The control scheme based on a SRF-PI regulator is shown in Fig. 3. Similarly to the scheme presented in Section III, this one includes a feedforward action (with $K_f = 1$) [3] and a feedback loop in which a PI controller is used in a SRF.

The closed-loop transfer function can be obtained combining the transfer function of the plant shown in equation (8) with the following transfer function of a PI controller plus a phase-lag compensator. This compensation is necessary to reduce the amplitude of the frequency response at the resonant frequency caused by the LC filter

$$C_{\mathrm{PI}}(s) = \left(K_{\mathrm{p}} + K_{\mathrm{i}} \frac{1}{s} \right) \frac{\omega_{\mathrm{cut}}}{s + \omega_{\mathrm{cut}}}, \tag{18}$$

where K_{p} and K_{i} are the proportional and integral gains, respectively, and ω_{cut} is the pole modulus of the phase-lag compensator.

The resulting closed-loop transfer function is therefore

$$F(s) = \frac{sK_{\mathrm{p}}\omega_{\mathrm{n}}^2\omega_{\mathrm{cut}} + K_{\mathrm{i}}\omega_{\mathrm{n}}^2\omega_{\mathrm{cut}}}{s^4 + As^3 + Bs^2 + Cs + D}, \tag{19}$$

with:

$$A = 2\xi\omega_{\mathrm{n}} + \omega_{\mathrm{cut}},\ B = \omega_{\mathrm{n}}^2 + 2\xi\omega_{\mathrm{n}}\omega_{\mathrm{cut}},$$
$$C = \omega_{\mathrm{n}}^2\omega_{\mathrm{cut}}\left(1 + K_{\mathrm{p}}\right),\ D = K_{\mathrm{i}}\omega_{\mathrm{n}}^2\omega_{\mathrm{cut}}. \tag{20}$$

Equation (19) yields $|F(0)| = 1$ and $\angle F(0) = 0°$, for any positive value of the parameters K_{p} and K_{i}. After analysing the root locus, the controller parameters which give a good tradeoff between control speed, stability and accuracy are: $K_{\mathrm{p}} = 0.0033$, $K_{\mathrm{i}} = 100$ and $\omega_{\mathrm{cut}} = 300$ rad/s. Fig. 6 shows the root locus of the control implemented. It can be observed that the dominant poles are located at ($s = -150 \pm \mathrm{j}85.8$), and therefore, the dynamic response will be slower when compared to the GPI control scheme. It should be remarked that increasing the SRF-PI control bandwidth would lead to overshoots that could exceed the maximum allowed voltage in the protected load.

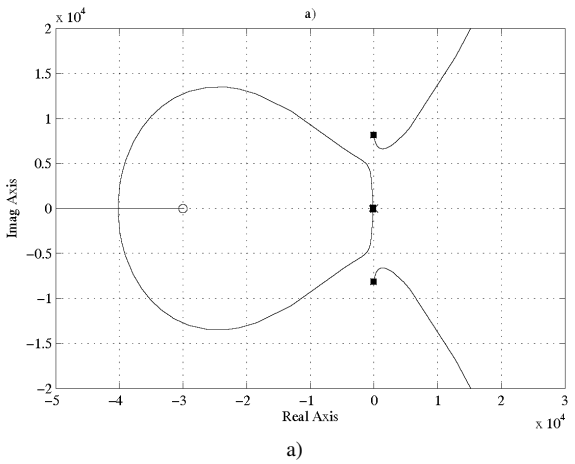

a)

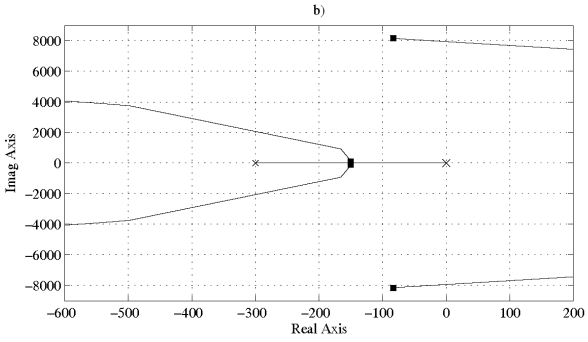

b)

Fig. 6. Root-locus plot for the designed SRF-PI control scheme (a) and Detail of the root-locus plot (b).

Fig. 7 shows the Bode plot of the designed SRF-PI control scheme.

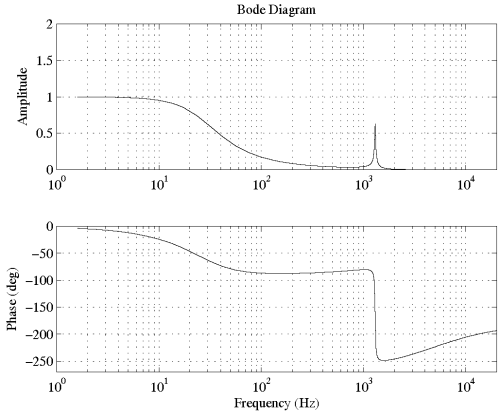

Fig. 7. Bode plot of the closed-loop system for the SRF-PI control scheme.

V. SIMULATION RESULTS

In order to test the performance of both control strategies designed in the previous sections, extensive simulation results have been performed using PSCAD/EMTDC. The test system implemented is shown in Fig. 8. It consists of two linear loads connected to the PCC: an induction motor and a sensitive load consisting in a three-phase star-connected RL load, which is protected by the DVR. The DVR is composed by three H-bridge-topology converters, a coupling transformer and an output capacitor. The dc voltage of the VSC was set to 600 V. The most relevant parameters used in simulations are summarized in Table I.

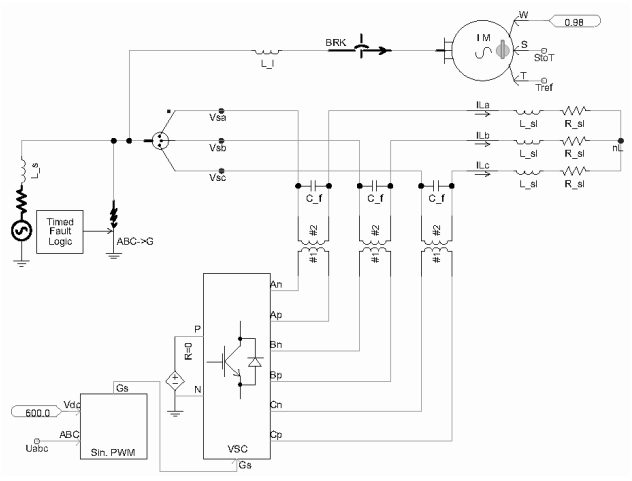

Fig. 8. Study case implemented using PSCAD/EMTDC.

TABLE I. PARAMETERS OF THE TEST SYSTEM.

Electrical Grid	Rated line-to-line voltage: 400 V Frequency: 50 Hz
Grid Impedance	Resistance: R_s = 11 mΩ Inductance: L_s = 0,6 mH
Induction Motor	Line inductance: L_l = 0,5 μH Rated active power: P_e = 11 kW Rated voltage: V_{nom} = 400 V
Sensitive Load:	Resistance: R_{sl} = 2.8 Ω Inductance: L_{sl} = 48 mH
Coupling Transformers	Rated apparent power: S = 20 kVA Rated voltage windings: 400 V/400 V Winding resistance: R_f = 0,6 Ω Leakage inductance: L_f = 2,8 mH Magnetising inductance has been neglected
Output Filter	Capacitor: C_f = 4,7 μF Cutoff frequency: f_c = 1387 Hz
Voltage-Source-Converter	Switching frequency: 7350 Hz Three VSC with H-bridge topology have been used

The DVR is always protecting the sensitive load with the following sequence of events: from $t = 0.1\,\text{s}$ to $t = 0.3\,\text{s}$ a 20% imbalanced voltage sag takes place as a consequence of a short-circuit fault at the PCC involving phases A and C. The squirrel-cage induction motor is started at $t = 0.4\,\text{s}$, which produces a balanced voltage-sag at the PCC. The simulation finishes at $0.6\,\text{s}$.

The three line-to-neutral voltages measured in the PCC when the imbalanced voltage sag occurs are shown in Fig. 9.

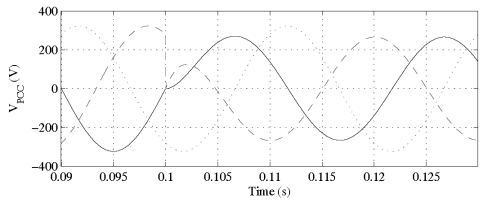

Fig. 9. Imbalanced-voltage-sag case: line-to-neutral voltages at the PCC, from $t = 0.09\,\text{s}$ to $t = 0.13\,\text{s}$.

Fig. 10 and Fig. 11 show the line-to-neutral voltages measured in the sensitive load obtained with the SRF-GPI control and the SRF-PI control, respectively, and the reference voltages that should be tracked by the control. It can be seen that both control strategies ameliorate the imbalanced voltage sag, but the transient response of the SRF-GPI control is faster when compared to the response obtained by the SRF-PI controller. Moreover, the accuracy of the SRF-GPI control scheme is better in steady state.

The performance of both control systems in case of a balanced voltage sag from *t*=0.39 s to *t*=0.43 s is shown in Fig. 12. As it is shown, both controllers exhibit an excellent reference tracking when the balanced voltage sag occurs. It should be remarked that the SRF-PI control performs better when compared to the imbalanced case.

The last test carried out shows the behavior of both control strategies when the grid frequency experiences a 10% reduction from its nominal value, i.e. from 50 Hz to 45 Hz. As shown in Fig. 13, both control schemes are able to ameliorate the imbalanced voltage sag. However, it is important to emphasize that again the behavior of the SRF-GPI control scheme overcomes the performance obtained with the SRF-PI controller.

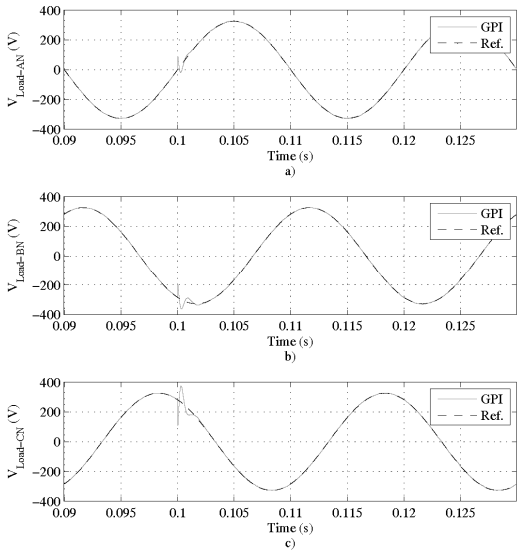

Fig. 10. Imbalanced-voltage-sag case: line-to-neutral voltages in the sensitive load obtained with the SRF-GPI controller, from $t = 0.09\,\text{s}$ to $t = 0.13\,\text{s}$, a) $V_{Load-AN}$ b) $V_{Load-BN}$ and c) $V_{Load-CN}$.

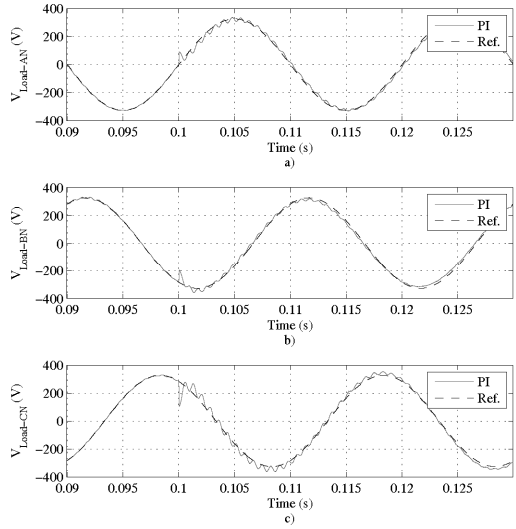

Fig. 11. Imbalanced-voltage-sag case: line-to-neutral voltages in the sensitive load obtained with the SRF-PI controller, from $t = 0.09\,\text{s}$ to $t = 0.13\,\text{s}$, a) $V_{Load-AN}$ b) $V_{Load-BN}$ and c) $V_{Load-CN}$.

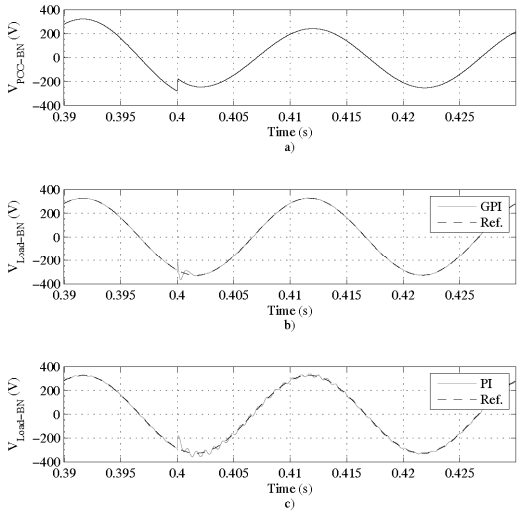

Fig. 12. Balanced-voltage-sag case: line-to-neutral voltages at the PCC and in the sensitive load at phase B from $t = 0.39\,\text{s}$ to $t = 0.43\,\text{s}$, a) V_{PCC-BN} b) $V_{Load-BN}$ and c) $V_{Load-BN}$.

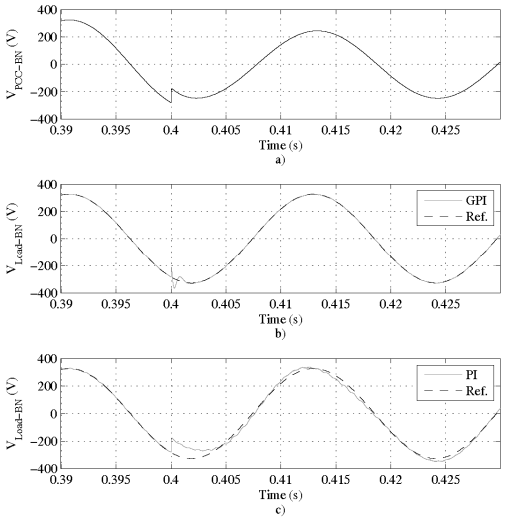

Fig. 13. Frequency deviation of -5 Hz with an imbalanced voltage sag at phase B: line-to-neutral voltages at the PCC and in the sensitive load from $t = 0.39\,\text{s}$ to $t = 0.43\,\text{s}$), a) V_{PCC-BN} b) $V_{Load-BN}$ and c) $V_{Load-BN}$.

Table II summarizes the 5% settling time of both control schemes for the different cases simulated. It is noteworthy that the settling time in each case depends not only on the dynamic response of the designed controllers and the filter, but also on the transient of the voltage-sag to be compensated. It can be seen that the transient response of the SRF-GPI scheme is faster than the one obtained with the SRF-PI scheme.

TABLE II. SETTLING TIME OF THE SRF-PI AND SRF-GPI CONTROL SCHEMES.

	Settling time (ms)	
	SRF-PI	**SRF-GPI**
Imbalanced Voltage Sag	8 ms	1.25 ms
Balanced Voltage Sag	8.5 ms	1.15 ms
Frequency deviation	4 ms	1.1 ms

VI. CONCLUSIONS

In this paper, two control schemes implemented in a SRF for the compensation of balanced and imbalanced voltage sags using a DVR system are presented. Both control strategies use a unity feedforward action and are implemented in a SRF. The SRF-GPI control uses a feedback loop with a GPI controller, while the SRF-PI control is based on a feedback loop with a conventional PI controller. An extensive comparison of the performance of both control methods for balanced and imbalanced voltage sags, including frequency deviations, is carried out in PSCAD/EMTDC. The results show that the performance achieved with the SRF-GPI controller is superior to the one obtained with the widely used SRF-PI controller in terms of dynamic response and steady-state accuracy, particularly when the voltage sag is imbalanced. Both methods provide a robust response to frequency deviations, being the performance of the SRF-GPI control scheme superior once again when compared to the results obtained with the SRF-PI control scheme.

REFERENCES

[1] H. J. Bollen, *Understanding Power Quality Problems: Voltage Sags and Interruptions*, Piscataway, NJ: IEEE Press, 2000.

[2] T. I. El-Shennawy, A. Moussa, M. A. El-Gammal, A. Y. Abou-Ghazala, "A dynamic voltage restorer for voltage sag mitigation in a refinery with induction motors loads", *American Journal of Engineering and Applied Sciences*, vol. 3, no. 1, pp. 144–151, 2010. [Online]. Available: http://dx.doi.org/10.3844/ajeassp.2010.144.151

[3] M. J. Newman, D. G. Holmes, J. G. Nielsen, F. Blaabjerg, "A dynamic voltage restorer (dvr) with selective harmonic compensation at medium voltage level," *IEEE Transactions on Industry Applications*, vol. 41, no. 6, pp. 1744–1753, Nov./Dec. 2005. [Online]. Available: http://dx.doi.org/10.1109/TIA.2005.858212

[4] Y. W. Li, P. C. Loh, F. Blaabjerg, D. M. Vilathgamuwa, "Investigation and improvement of transient response of dvr at medium voltage level", *IEEE Transactions on Industry Applications*, vol. 43, no. 5, pp. 1309–1319, Sept./Oct. 2007. [Online]. Available: http://dx.doi.org/10.1109/TIA.2007.904430

[5] P. Roncero-Sánchez, E. Acha, "Dynamic voltage restorer based on flying capacitor multilevel converters operated by repetitive control", *IEEE Transactions on Power Delivery*, vol. 24, no. 2, pp. 951–960, Apr. 2009. [Online]. Available: http://dx.doi.org/10.1109/TPWRD.2008.2005885

[6] A. Parreño Torres, P. Roncero-Sánchez, X. del Toro García, V. Feliu, "Generalized proportional-integral controller for dynamic voltage restorers", *COMPEL: The International Journal for Computation and Mathematics in Electrical and Electronic Engineering*, vol. 31, no. 6, pp. 1964–1984, 2012. [Online]. Available: http://dx.doi.org/10.1108/03321641211267236

[7] Y. Li, D. M. Vilathgamuwa, P. C. Loh, "Design, analysis, and real-time testing of a controller for multibus microgrid system", *IEEE Transactions on Power Electronics*, vol. 19, no. 5, pp. 1195–1204, Sep. 2004. [Online]. Available: http://dx.doi.org/10.1109/TPEL.2004.833456

[8] P. T. Cheng, J. C. Chen, C. L. Ni, "Design of a state-feedback controller for series voltage-sag compensators", *IEEE Transactions on Industry Applications*, vol. 45, no. 1, pp. 260–267, Jan./Feb. 2009. [Online]. Available: http://dx.doi.org/10.1109/TIA.2008.2009606

[9] H. Sira-Ramírez, "Sliding modes, delta-modulators, and generalized proportional integral control of linear systems", *Asian Journal of Control*, vol. 5, no. 4, pp. 467–475, Dec. 2003. [Online]. Available: http://dx.doi.org/10.1111/j.1934-6093.2003.tb00164.x

[10] R. Morales, V. Feliu, H. Sira-Ramírez, "Nonlinear control for magnetic levitation systems based on fast online algebraic identification of the input gain", *IEEE Transactions on Control Systems Technology*, vol. 19, no. 4, p. 757–771, Apr. 2011. [Online]. Available: http://dx.doi.org/10.1109/TCST.2010.2057511